



MIT Open Access Articles

Ultra#Uniform Nanocrystalline Materials via Two#Step Sintering

The MIT Faculty has made this article openly available. **Please share** how this access benefits you. Your story matters.

As Published	10.1002/ADFM.202007750
Publisher	Wiley
Version	Author's final manuscript
Citable link	https://hdl.handle.net/1721.1/133241
Terms of Use	Creative Commons Attribution-Noncommercial-Share Alike
Detailed Terms	http://creativecommons.org/licenses/by-nc-sa/4.0/

Ultra-Uniform Nanocrystalline Materials via Two-Step Sintering

Yanhao Dong, Hongbing Yang, Lin Zhang, Xingyu Li, Dong Ding, Xiaohui Wang, Ju Li,* Jiangong Li,* and I-Wei Chen*

Nanocrystalline materials with superior properties are of great interest. Much is discussed about obtaining nanograins, but little is known about maintaining grain-size uniformity that is critical for reliability. An especially intriguing question is whether it is possible to achieve a size distribution narrower than what Hillert theoretically predicted for normal grain growth, a possibility suggested—for growth with a higher growth exponent—by the generalized mean-field theory of Lifshitz, Slyozov, Wagner (LSW), and Hillert but never realized in practice. Following a rationally designed two-step sintering route, it has been made possible in bulk materials by taking advantage of the large growth exponent in the intermediate sintering stage to form a uniform microstructure despite residual porosity, and freezing the grain growth thereafter while continuing densification to reach full density. The bulk dense Al_2O_3 ceramic thus obtained has an average grain size of 34 nm and a size distribution much narrower than Hillert's prediction. Bulk Al_2O_3 with a grain-size distribution narrower than the particle-size distribution of starting powders is also demonstrated, as are highly uniform bulk engineering metals (refractory Mo and W-Re alloy) and complex functional ceramics (BaTiO_3 -based alloys with superior dielectric strength and energy capacity).

(e.g., grain-boundary strengthening via the Hall-Petch relationship) are mainly attributed to the average grain size, it is the size distribution that matters most to engineering reliability.^[4,5] This is because mechanical, electrical, dielectric, and other failures dictated by instantaneous or gradual breakdown events typically happen at the weakest point, which is often associated with a microstructural or chemical inhomogeneity at some grain or grain boundary. Reducing grain size dispersion will make all grains alike, which tends to eliminate inhomogeneity. Therefore, it should be a major goal in nanomaterial development.

When all the grain boundaries have the same energy and mobility and cooperatively move to lower the total grain-boundary energy in a polycrystal, it leads to a parabolic “normal” growth law, (grain size)² \approx time. According to Hillert's solution that follows the mean-field approach of Lifshitz, Slyozov, and Wagner (LSW),^[6–9]

1. Introduction


Rapid development in the past decades has provided nanocrystalline materials with improved and emerging properties (e.g., mechanical strength, hardness, fracture toughness and stored dielectric energy).^[1–3] While the benefits of nanostructuring

the theoretical ratio σ , which is the ratio of the standard deviation Σ of the grain-size distribution to the average grain size G_{avg} , should be 0.354 in normal grain growth. Since real materials do not have grain boundaries of the same energy and mobility, they should have a larger σ during grain growth, which is true for a large number of dense ceramics sintered in

Dr. Y. Dong, Prof. Ju Li
Department of Nuclear Science and Engineering
Massachusetts Institute of Technology
Cambridge, MA 02139, USA
E-mail: liju@mit.edu

H. Yang, Prof. Jiangong Li
Institute of Materials Science and Engineering and
MOE Key Laboratory for Special Functional
Materials and Structure Design
Lanzhou University
Lanzhou 730000, China
E-mail: lijg@lzu.edu.cn

Prof. L. Zhang, X. Li
Beijing Advanced Innovation Center for Materials Genome Engineering
Institute for Advanced Materials and Technology
University of Science and Technology Beijing
Beijing 100083, China

 The ORCID identification number(s) for the author(s) of this article can be found under <https://doi.org/10.1002/adfm.202007750>.

Dr. D. Ding
Energy and Environmental Science and Technology
Idaho National Laboratory
Idaho Falls, ID 83415, USA

Prof. X. Wang
State Key Laboratory of New Ceramics and Fine Processing
School of Materials Science and Engineering
Tsinghua University
Beijing 100084, China

Prof. Ju Li
Department of Materials Science and Engineering
Massachusetts Institute of Technology
Cambridge, MA 02139, USA

Prof. I-W. Chen
Department of Materials Science and Engineering
University of Pennsylvania
Philadelphia, PA 19104, USA
E-mail: iweichen@seas.upenn.edu

DOI: 10.1002/adfm.202007750

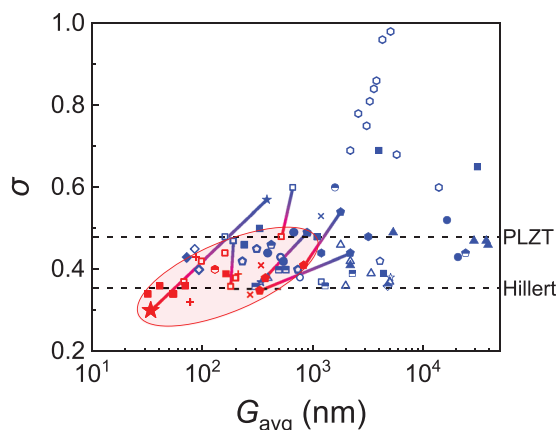


Figure 1. “Quality plot” of G_{avg} and σ of sintered materials. G_{avg} and σ of 25 dense bulk materials represented by 24 different types of symbols listed in Table S1, Supporting Information, variously sintered as reported in the literature and in this work. Two-step sintered in red, conventionally sintered in blue, and those by both methods (all in this work except for W) with the same powders and green body forming treatment are connected by solid lines. Lower dashed line: Hillert’s theoretical prediction.^[6] Upper dashed line: hot-pressed transparent (Pb,La)(Zr,Ti)O₃ (PLZT) with a known uniform microstructure.^[30] Shaded ellipse is for guidance of eyes.

various ways^[4,10–45] as shown by the blue data points in **Figure 1**. Meanwhile, **Figure 1** also reveals that smaller σ tends to come with a smaller G_{avg} . This trend explains why nanomaterials are attractive: they tend to combine small G_{avg} and small σ , which is the key to exceptional properties and reliability. Thus, the state of the art suggests that there is a lower limit of grain-size dispersion set by Hillert’s $\sigma = 0.354$, and it would be difficult, if not impossible, to do better in real dense materials. But if a better nanomaterial is to come, one must challenge this limit and find a way to obtain bulk, dense engineering nanomaterials with a smaller σ . We will demonstrate that this is possible by taking advantage of a growth stagnation in intermediate-stage sintering.

2. Theoretical Reasoning from Generalized Growth Law

To motivate our approach, we recall that essentially monosized nanoparticles are routinely obtained by liquid-phase precipitation after proper growth and coarsening—also called Ostwald ripening, and this paradigm is relevant to bulk sintering because Ostwald ripening is described by the same LSW theory.^[7,8,46,47] The common rationale is that particle-size evolution is a self-sharpening process due to the rapid decay of growth rate with size. This growth/coarsening stagnation is caused by a) a diminishing driving force (capillary pressure) that inversely scales with the particle size and b) a diminishing diffusion kinetics that has a diffusion distance proportional to the particle size. Mathematically, a faster approach to stagnation is signaled by a higher exponent of the growth law, (particle/grain size) ^{n} \approx time, where n is 3 in Oswald ripening and 2 in normal grain growth. Inasmuch as σ decreases with n , one stands to reason that if a higher growth exponent can somehow be engineered into sintering, then it would be possible to

obtain a more uniform sintered microstructure than that predicted by Hillert. This will yield a better nanomaterial that lies closer to the lower-left corner of **Figure 1**: one with “ultra-fine” and “ultra-uniform” grains. How to achieve it in theory and in practice is illustrated below for a dense bulk Al₂O₃ ceramic with $G_{\text{avg}} = 34$ nm and $\sigma = 0.30$, indicated by the red star in **Figure 1**. Other small- σ materials of practical interest obtained by the same method will also be described.

Our reasoning is supported by the analytic solution of steady-state size distribution for the generalized LSW-Hillert growth equation,^[9]

$$\frac{dG}{dt} = 2M\gamma \left(\frac{G}{a} \right)^{\alpha} \left(\frac{1}{G_{\text{cr}}} - \frac{1}{G} \right) \quad (1)$$

Here, G is the size of a growing or shrinking grain/particle, M is the mobility, γ is the interfacial energy, a is a length (e.g., atomic spacing) that preserves the dimension, $2\gamma/G$ is the capillary pressure, and G_{cr} is the critical size of a grain/particle that neither grows nor shrinks at time t —thereby setting a chemical potential (in pressure) $2\gamma/G_{\text{cr}}$ for the system that ensures mass/volume conservation at t . More specifically, M is the grain boundary mobility in normal grain growth, and $M = \frac{D}{k_B T} \frac{\Omega}{a}$ (with D the diffusivity, Ω the atomic volume, k_B the Boltzmann constant and T the absolute temperature) in particle growth. The different growth dynamics signaled by n comes from α , which is 0 in normal grain growth and -1 in LSW (Ostwald ripening). For an arbitrary $\alpha \leq 1$, we obtained a steady-state power-law $G_{\text{avg}}^n \approx t$ with a growth exponent $n = 2 - \alpha \geq 1$, and a close form solution^[9] of the normalized size distribution $P(u)$ for $u = G/G_{\text{cr}}$

$$P'(u) = \frac{3u^{1-\alpha}}{u^{2-\alpha} - \frac{(2-\alpha)^{2-\alpha}}{(1-\alpha)^{1-\alpha}}(u-1)} \exp \left[-\frac{3}{2-\alpha} \int_0^u \frac{-(2-\alpha)u^{1-\alpha}}{(2-\alpha)^{2-\alpha}(u-1) - u^{2-\alpha}} du \right] \quad (2)$$

A more convenient distribution $P(G/G_{\text{avg}})$ in terms of the normalized grain size G/G_{avg} is obtained from $u = \frac{G}{G_{\text{avg}}} u_{\text{avg}}$, where $u_{\text{avg}} = \int_0^{u_0} u P'(u) du$ with u_0 being the upper cutoff of the distribution. **Figure 2** clearly illustrates that $P(G/G_{\text{avg}})$ sharpens as α decreases and n increases; meanwhile, its $\sigma = \Sigma/G_{\text{avg}}$ (where Σ is the standard deviation of G) decreases as shown in the inset of **Figure 2**. Clearly, to beat Hillert’s $\sigma = 0.354$ limit, one must find an $\alpha < 0$ ($n > 2$) process to replace normal grain growth.

Normal grain growth with $n = 2$ was firmly established in dense ceramics, for example, in undoped or variously doped Y₂O₃, CeO₂, and ZrO₂.^[20,21,38] However, it is known that the grain-growth exponent $n \geq 3$ in porous ceramics. This is because the grain boundaries of a larger grain are statistically in contact with more pores, hence sense stronger pinning forces.^[48] The latter applies to intermediate-stage sintering, defined as sintering of a powder compact in which already-neck-bonded particles are still separated by mostly open porosity (namely, interconnected pore channels) instead of isolated pores as in final-stage sintering. Therefore, we hypothesized that σ of the

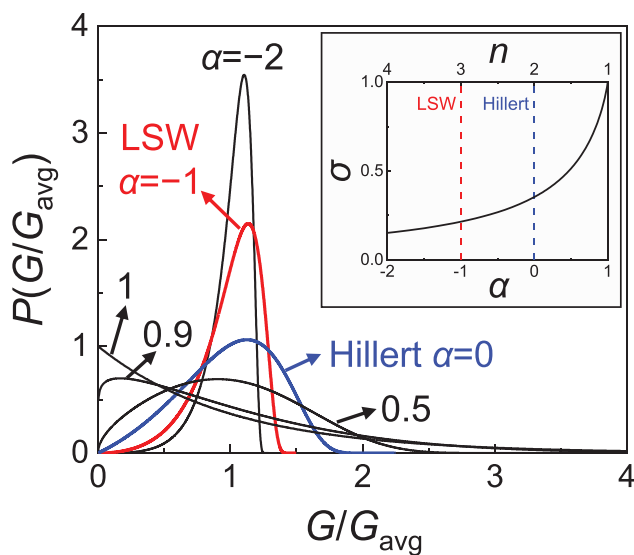


Figure 2. Steady-state solution of generalized growth equation. Calculated normalized grain size distribution $P(G/G_{\text{avg}})$ as a function of α . Inset: Calculated standard deviations σ for G/G_{avg} as a function of α and n .

intermediate-stage microstructure is smaller than Hillert's 0.354, and if the hypothesis is verified, we hoped such a state could provide a "template" to grow materials with unprecedented uniformity.

3. Capturing Ultra-Uniform Microstructure during Intermediate-Stage Sintering

To verify the hypothesis, we sintered powder compacts made of 4.7 nm high-purity Al_2O_3 powders without applied pressure, that is, by free sintering. After reaching a set temperature, the partially dense compact was immediately cooled and analyzed. (See Section 7 for experimental details.) Although a higher set temperature always led to a higher relative density ρ , as well as larger G_{avg} (open circles in Figure 3a) and Σ (error bar), both measured from the transmission electron microscopy (TEM) images of fractured fragments, the variation of σ (open circles in Figure 3c) is non-monotonic and reaches a minimum at $\rho = 65\%$. This density with the smallest σ will be called ρ_u , where the subscript "u" stands for "uniform". The same trend was confirmed by the data in Figure 3b (G_{avg} as filled circles and Σ as error bars) and Figure 3c (σ as filled circles) measured from scanning electron microscopy (SEM) images of fractured and thermally etched surfaces of the same set of samples. Since σ during much of the $\rho = 60$ –85% range falls significantly below Hillert's $\sigma = 0.354$ (dashed horizontal line in Figure 3c), our hypothesis is confirmed.

Uniform intermediate-stage microstructure is evident from the micrograph and grain-size histogram of an Al_2O_3 sample with $\sigma = 0.31$ at $\rho = 84\%$, shown in Figure 4a,b, taken from the SEM images of fractured and thermally etched surfaces. Comparably small σ values were also obtained in other free-sintered porous ceramics, 8 mol% yttria-stabilized cubic zirconia (8YSZ) with $\sigma = 0.30$ (orange square in Figure 3c, measured from the SEM images of polished and thermally etched surfaces) at

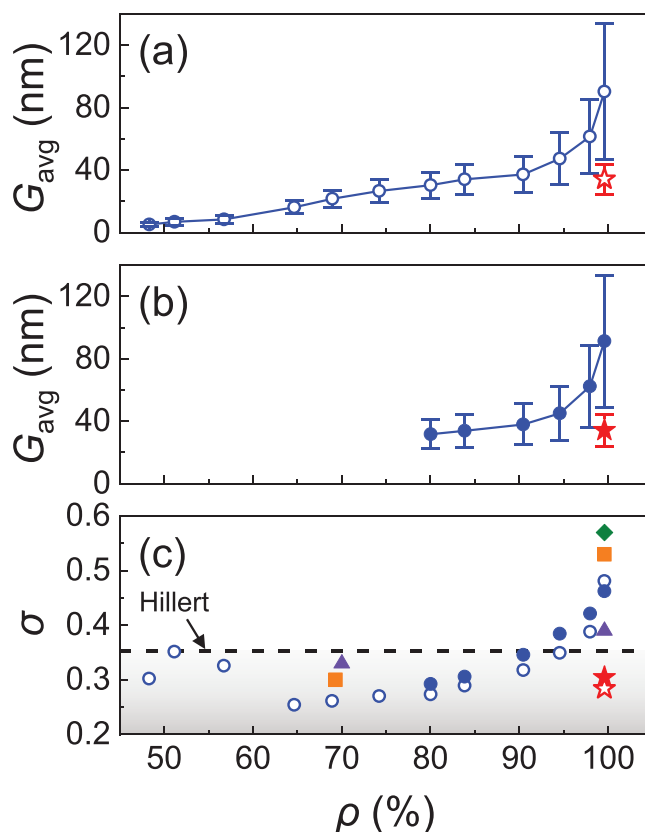


Figure 3. Microstructural dispersity in porous and dense polycrystals. Trajectory of average grain size G_{avg} versus relative density ρ of Al_2O_3 ceramics measured under a) TEM in open symbols and b) SEM in closed symbols, with standard deviation Σ shown as error bars. Two-step sintering data at full density also plotted as stars. c) Relative standard deviation, $\sigma = \Sigma/G_{\text{avg}}$, from a,b) using the same symbols. Also included are orange square (8YSZ) at $\rho = 69\%$ and purple triangle (3YSZ) at $\rho = 70\%$; orange square (8YSZ), purple triangle (3YSZ), and green diamond (Al_2O_3) at $\rho \approx 100\%$: the latter samples annealed for additional time at highest temperature after reaching nearly full density. (See text for details.)

$\rho = 69\% \approx \rho_u$, and 3 mol% yttria-stabilized tetragonal zirconia (3YSZ) with $\sigma = 0.33$ (purple triangle in Figure 3c, measured from the SEM images of polished and thermally etched surfaces) at $\rho = 70\% \approx \rho_u$. Their micrographs and grain size histograms (Figure 4c,d for 8YSZ and Figure 4e,f for 3YSZ) all portray a highly uniform microstructure despite the prominent presence of open pore channels.

4. Preserving Microstructural Uniformity to Full Density via Two-Step Sintering

Unfortunately, although a remarkably small σ throughout the intermediate-stage sintering is now established, the uniformity invariably deteriorates as most open porosity is eliminated—especially when density exceeds 90% (see Figure 3c) that marks the onset of final-stage sintering in most materials.^[49,50] The common practice of holding the material at the highest sintering temperature for additional time to assure full densification makes matters worse, as it causes concurrent

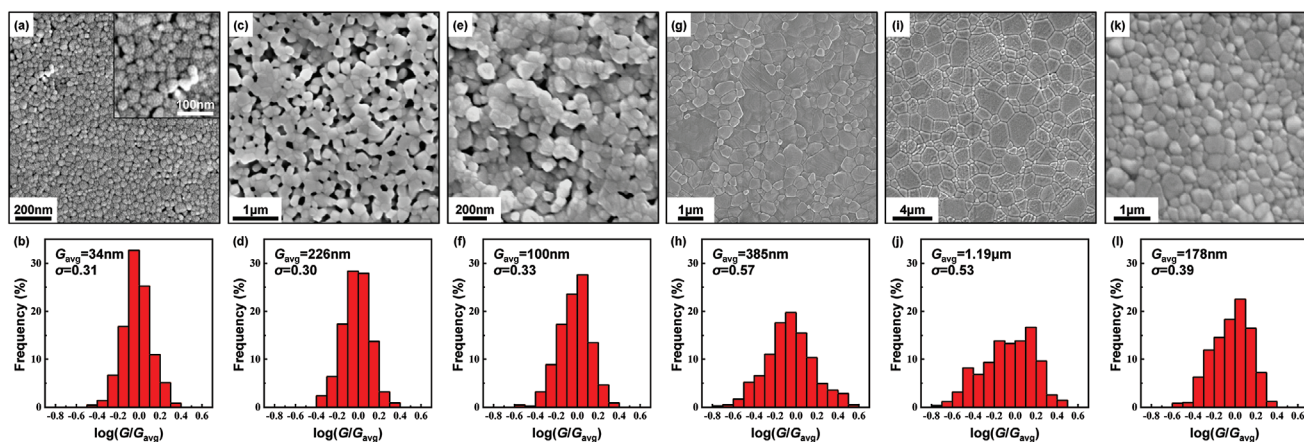


Figure 4. Comparing microstructural uniformity in porous and dense ceramics. SEM micrographs and normalized grain size histograms of a,b) Al_2O_3 heated to 1150 °C without holding, $\rho = 84\%$; inset in (a): enlarged section showing porosity; c,d) 8YSZ heated to 1280 °C without holding, $\rho = 69\%$; e,f) 3YSZ heated to 1240 °C without holding, $\rho = 70\%$; g,h) dense Al_2O_3 sintered at 1300 °C for 10 h; i,j) dense 8YSZ sintered at 1300 °C for 12 h; and k,l) dense 3YSZ sintered at 1300 °C for 12 h. Also listed in histograms are G_{avg} and σ .

grain growth in nearly dense materials that increases σ further. For example, σ reached 0.57 in an Al_2O_3 ceramic (measured from the SEM images of fractured and thermally etched surfaces) held for 10 h at 1300 °C as indicated by the green diamond at $\rho = 100\%$ in Figure 3c. It has a visibly deteriorated microstructure (Figure 4g) and a much less uniform grain-size histogram (Figure 4h) than its $\rho = 84\%$ predecessor (Figure 4a,b). The same holds for 8YSZ and 3YSZ held at 1300 °C for 12 h: they feature much larger σ (0.53 for 8YSZ, orange square at $\rho \approx 100\%$ in Figure 3c; 0.39 for 3YSZ, purple triangle at $\rho \approx 100\%$ in Figure 3c; both measured from the SEM images of polished and thermally etched surfaces) and visibly worse microstructures (Figure 4i,l) than their porous counterparts in Figure 4c,f. Among them, 3YSZ experienced the least deterioration after high-temperature holding. This is because it is endowed with a strong solute drag that increases grain-growth resistance (which is why it is the first and best superplastic ceramic^[51]). Yet its σ still increased from 0.33 to 0.39 as G_{avg} grew from 100 nm at $\rho = 70\%$ to 178 nm after holding at 1300 °C (Figure 4f,l).

Clearly, a different sintering strategy is needed to retain the uniform intermediate-stage microstructure during densification. Two-step sintering^[52] has been shown to do exactly that: it effects densification (via diffusion along stationary grain boundaries, which requires a relatively small activation energy) without grain growth (via grain-boundary migration that must perturb the grain-boundary network, which requires a relatively large activation energy). In this way, two-step sintering keeps the microstructure frozen while improving the density, and in the past 20 years it has been successfully demonstrated in numerous oxides, nitrides, carbides and some metals.^[15–17,36,37,43–45,52–56] In practice, it first heats the powder compact to a higher temperature (designated as T_1) without holding to attain a high enough density, then lowers the temperature to T_2 and holds there for an extended time to reach full density. To succeed, the post- T_1 density should be high enough to render all remaining pores/pore channels unstable, which requires their surface curvatures to change from negative to positive (a spherical pore has a uniformly positive surface curvature of $2/\text{radius}$). With 4.7 nm Al_2O_3 powders ($G_{avg} = 4.7$ nm

and $\sigma = 0.23$ measured from the TEM images of dispersed powders; TEM micrograph and normalized grain size histogram in Figure 5a,b), we used $T_1 = 1150$ °C to reach $\rho = 84\%$, then cooled the sample down to $T_2 = 1025$ °C with an additional hold for 40 h to obtain a final density of 99.6%. As shown by the microstructure in Figure 5c and the grain size histogram in Figure 5d, the dense body has essentially the same G_{avg} (34 nm, measured from the SEM images of fractured and thermally etched surfaces; also shown in Figure 3a,b by stars, open ones from TEM and filled ones from SEM) and σ (0.30 from SEM; shown in Figure 3c from red error bars in Figure 3a,b) as those of the $\rho = 84\%$ sample (post- T_1 and before cooling down to T_2 , $G_{avg} = 34$ nm and $\sigma = 0.30$, Figure 4a,b). Therefore, the second step not only arrests grain growth, but also preserves grain-size uniformity. Having successfully frozen the microstructure throughout T_2 -sintering, we obtained a dense nanocrystalline bulk ceramic—the red star in Figure 1—an “ultra-uniform” alumina, thus called because its $\sigma = 0.30$ lies below Hillert’s limit.

Two-step free sintering also led to other bulk materials more uniform than possible by conventional sintering. As shown in Figure 6a,b, two-step sintered bulk Mo ($T_1 = 1180$ °C for 1 h, $T_2 = 1110$ °C for 10 h) has a finer and more uniform microstructure ($G_{avg} = 370$ nm and $\sigma = 0.38$) than conventionally sintered Mo (1400 °C for 3 h) in Figure 6c,d that has $G_{avg} = 890$ nm and $\sigma = 0.49$. Likewise, two-step sintered 90W-10Re alloy ($T_1 = 1200$ °C for 1 h, $T_2 = 1100$ °C for 20 h) shown in Figure 6e,f has a finer and more uniform microstructure ($G_{avg} = 330$ nm and $\sigma = 0.35$) than conventionally sintered 90W-10Re (1500 °C for 2 h) in Figure 6g,h that has $G_{avg} = 2.2$ μm and $\sigma = 0.44$. These examples demonstrate that two-step free sintering can obtain bulk metals and alloys of extremely high melting points (2623 °C for Mo and ≈ 3200 °C for 90W-10Re). This is especially note-worthy because it used unusually low sintering temperatures (≤ 1200 °C) and no low-melting-point sintering aid, which would have caused possible contamination and deleterious effects on properties.

Two-step free sintering was further used to densify complex perovskites derived from $BaTiO_3$, which is the basis of commercially important ceramic capacitors. As shown in Figure 6i,j the microstructure of two-step sintered $BaTiO_3$ ($T_1 = 1250$ °C for

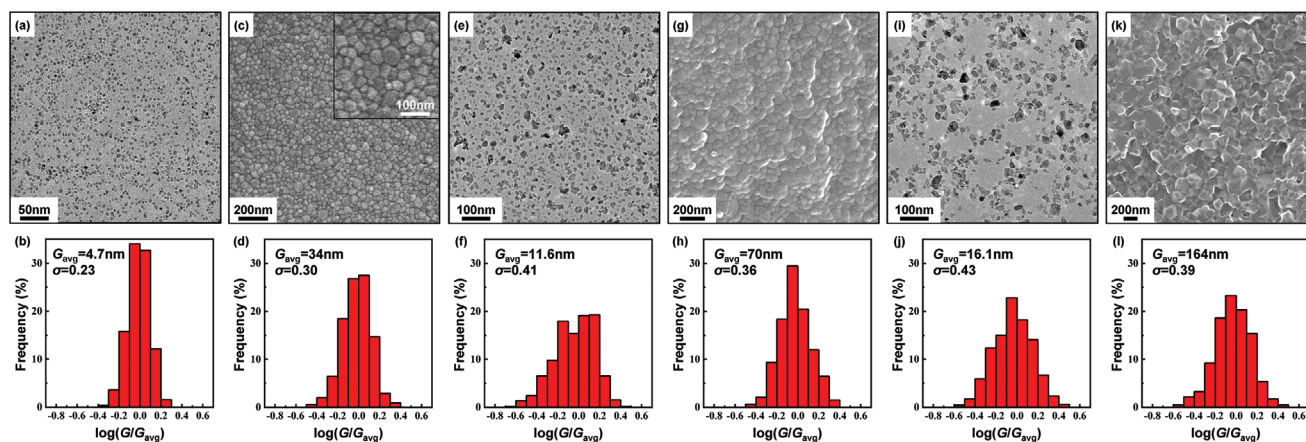


Figure 5. Two-step sintered nanocrystalline bulk Al_2O_3 with different starting powders. Micrographs and normalized grain size histograms of a,b) 4.7 nm Al_2O_3 powders and c,d) dense two-step sintered Al_2O_3 reaching 1150 °C (T_1) without holding and then held at 1025 °C (T_2) for 40 h using 4.7 nm Al_2O_3 powders; inset in (c): enlarged section showing absence of porosity. Corresponding micrographs and histograms of e,f) 11.6 nm Al_2O_3 powders and g,h) dense two-step sintered Al_2O_3 reaching 1200 °C (T_1) without holding and then held at 1000 °C (T_2) for 20 h using 11.6 nm Al_2O_3 powders. Similar micrographs and histograms of i,j) 16.1 nm Al_2O_3 powders and k,l) dense two-step sintered Al_2O_3 reaching 1275 °C (T_1) without holding and then held at 1075 °C (T_2) for 20 h using 16.1 nm Al_2O_3 powders. Also listed in histograms are G_{avg} and σ .

1 min, $T_2 = 1050^\circ\text{C}$ for 5 h) is more uniform ($G_{\text{avg}} = 180$ nm and $\sigma = 0.36$) than that of conventionally sintered one (1210 °C for 2 h, $G_{\text{avg}} = 190$ nm and $\sigma = 0.47$, Figure 6k,l), the latter having some abnormally large grains (Figure 6k) not found in Figure 6i. Such uniformity is directly correlated to a 4× better retention time in field-holding tests at 185 °C for the two-step sintered ceramic.^[4] Note that the BaTiO_3 powder used here was precoated with mixed dopant oxides of Ca, Ba, Y, Mg, Si, Mn, and Ho to form a core-shell structure, which is needed to suppress leakage current and to smooth out BaTiO_3 's ferroelectric transitions at 120 and 8 °C, thus providing a broad, temperature-insensitive and low-loss dielectric response required for multilayer ceramic capacitor (MLCC) applications. By suppressing the migration of grain boundaries that would have availed their fast-diffusing paths to dopant interdiffusion thus compromised the core-shell structure, two-step sintering can better maintain property advantages. Another perovskite of $0.87\text{BaTiO}_3\text{-}0.13\text{Bi}(\text{Zn}_{2/3}(\text{Nb}_{0.85}\text{Ta}_{0.15})_{1/3})\text{O}_3$ (BT-BZNT) composition was also two-step sintered ($T_1 = 1190$ °C for 1 min, $T_2 = 1040$ °C for 3 h) to obtain a microstructure ($G_{\text{avg}} = 520$ nm and $\sigma = 0.48$, Figure 6m,n) more uniform than obtained from conventional sintering (1150 °C for 3 h, $G_{\text{avg}} = 660$ nm and $\sigma = 0.60$, Figure 6o,p), where the latter also resulted in some abnormal grain growth not seen in the former. The better uniformity is directly correlated to a higher electrical field breakdown strength, which allows it to be fabricated into MLCCs (by the same two-step sintering procedure) that stored a record-high density of dielectric energy.^[57]

Previous sintering studies of density and pore/particle/grain-size evolutions found that σ of open pores, as well as the size ratio of pore-to-grain, decrease rapidly during initial-stage sintering.^[58,59] This was attributed to powder coarsening and neck formation, driven by surface diffusion, which in turn triggers particle relocation leading to homogenization of microstructure. These processes end when the powder compact becomes locked, which for spheres of the same size happens at $\rho_{\text{tcp}} = 0.63$ —the density of random close-packing—and usually at a somewhat

higher density if particle sizes vary. Still driven by surface diffusion, further grain coarsening relative to pores eventually renders all pores thermodynamically unstable, which occurs at a higher density ρ_c . After ρ_c , grain-boundary diffusion alone can drive densification all the way to full density, albeit at the cost of increasing σ of relative grain size unless two-step sintering is practiced. We suggest that particle/grain homogenization and locking can also explain why σ of relative grain size reaches a minimum in Figure 3, which occurs at $\rho_u = 0.65$ that is just slightly above ρ_{tcp} . If so, homogenization during initial-stage sintering followed by microstructure freezing during two-step sintering will allow a dense microstructure with a relatively small final σ , even if the starting powder compact has a relatively large σ .

To test this idea, we used an Al_2O_3 powder ($G_{\text{avg}} = 11.6$ nm and $\sigma = 0.41$, measured from the TEM images of dispersed powders; TEM micrograph and normalized grain size histogram in Figure 5e,f) less uniform than the one in the above example of Al_2O_3 ($\sigma = 0.23$ for the powder) to sinter an intermediate sample of $\rho = 84\%$ at $T_1 = 1200$ °C and a final sample of $\rho = 99.1\%$ with $G_{\text{avg}} = 70$ nm and $\sigma = 0.36$ (all measured from the SEM images of fractured and thermally etched surfaces; microstructure and normalized grain size histogram in Figure 5g,h) after holding at $T_2 = 1000$ °C for 20 h. Similarly, with another Al_2O_3 powder ($G_{\text{avg}} = 16.1$ nm, and $\sigma = 0.43$ measured from the TEM images of dispersed powders; TEM micrograph and normalized grain size histogram in Figure 5i,j), we used $T_1 = 1275$ °C to reach $\rho = 87\%$, and $T_2 = 1075$ °C for 20 h to obtain a 98.9% dense Al_2O_3 with $G_{\text{avg}} = 164$ nm and $\sigma = 0.39$ (measured from the SEM images of fractured and thermally etched surfaces; microstructure and normalized grain size histogram in Figure 5k,l). These ceramics having a final σ smaller than powder's initial σ support the idea that the σ evolutions of the relative grain size and relative pore size are a twin-measure of the homogenization process throughout initial- and intermediate-stage sintering,^[58,59] and they reach their lowest at $\rho_u \approx \rho_{\text{tcp}}$ when the porous compact becomes locked. After that two-step sintering must be used to preserve the uniform microstructure to higher density.

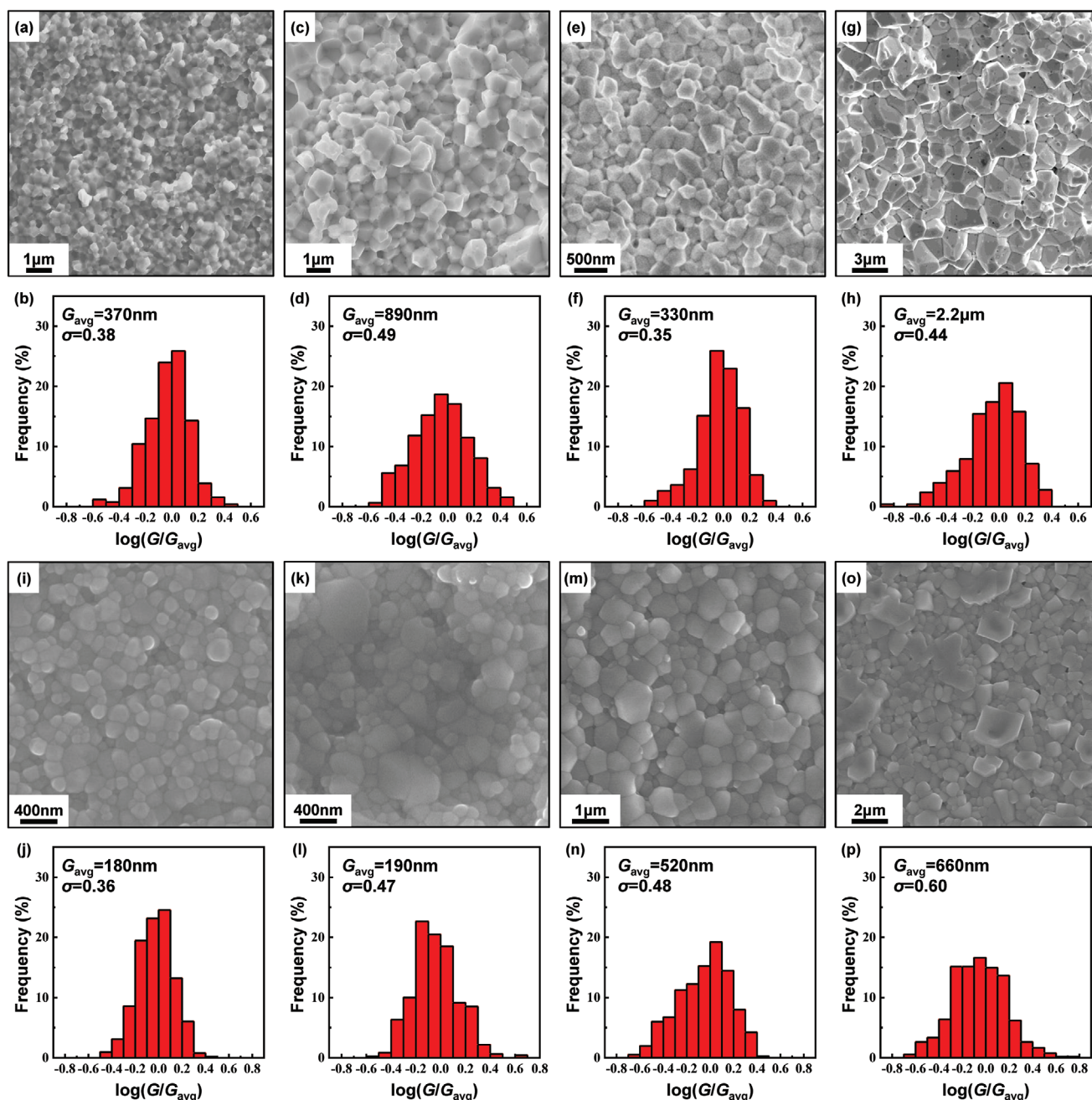


Figure 6. Two-step free-sintered ultrafine-grained bulk refractory metals and perovskite capacitors with uniform microstructure. Micrographs and normalized grain size histograms of a,b) dense two-step sintered Mo held at 1180 °C (T_1) for 1 h and then held at 1110 °C (T_2) for 10 h, compared to c,d) Mo conventionally sintered at 1400 °C for 3 h; e,f) dense two-step sintered 90W-10Re held at 1200 °C (T_1) for 1 h and then held at 1100 °C (T_2) for 20 h, compared to g,h) 90W-10Re conventionally sintered at 1500 °C for 2 h; i,j) dense two-step sintered BaTiO₃ (BT) held at 1250 °C (T_1) for 1 min and then held at 1050 °C (T_2) for 5 h, compared to k,l) conventionally sintered BT sintered at 1210 °C for 2 h; m,n) dense two-step sintered 0.87BaTiO₃-0.13Bi(Zn_{2/3}(Nb_{0.85}Ta_{0.15})_{1/3})O₃ (BT-BZNT) held at 1190 °C (T_1) for 1 min and then held at 1040 °C (T_2) for 3 h, compared to o,p) conventionally sintered BT-BZNT at 1150 °C for 3 h. Also listed in histograms are G_{avg} and σ .

5. Design Criteria for Best Two-Step Sintering Practice and Their Scientific Basis

Our findings can be used to guide best practices for two-step sintering. Existing data suggest that ρ_c , which signals a critical ratio of grain size to pore size above which pore shrinkage

is thermodynamically feasible without any grain-boundary movement, is similar for all cubic materials: $\approx 75\%$ in Y₂O₃,^[52,53] $\approx 73\%$ in BaTiO₃,^[17] $\approx 76\%$ in Ni_{0.2}Cu_{0.2}Zn_{0.6}Fe₂O₄.^[17] In contrast, Al₂O₃ is hexagonal with highly anisotropic interfacial energies, which is reflected in a dihedral-angle distribution from 76° to 166° (although this can be partially ameliorated

by doping)^[60] that is much more dispersed than seen in Y_2O_3 (88°–132°).^[58] So a much higher ρ_c of $\approx 83\%$ ^[16,56] is needed in Al_2O_3 to render pores with the least favorable dihedral angles thermodynamically unstable. Since ρ_c already exceeds ρ_u (where G_{avg} is smaller and σ is the smallest), going from ρ_u to ρ_c before T_2 -sintering means more grain coarsening, and this must go the furthest in Al_2O_3 because it has the highest ρ_c . Indeed, we found the ratio of final G_{avg} to initial powder size ranges from 6 to 10 for Al_2O_3 , compared to 3–6 for Mo and 90W-10Re and <2 in BaTiO_3 -based ceramics, indicating Al_2O_3 is intrinsically more difficult to sinter. Clearly, the selection of T_1 must pay close attention to this aspect in order to best capture ρ_c and minimize grain coarsening before T_2 -sintering. Meanwhile, attention also needs to be paid to powder agglomeration and non-uniform packing because they can give rise to lower local density even after an overall ρ_c is reached, thus preventing densification during T_2 -sintering.

Turning to T_2 -sintering, T_2 has been empirically found by trial and error in the literature (typically 100–200 °C below T_1) to allow the densification of many materials without grain growth. However, in 8YSZ we have recently identified, for the first time, a transition temperature T_{tr} : 2-grain-controlled boundary migration above T_{tr} , and 3/4-grain-junction-controlled boundary migration below T_{tr} .^[45] Moreover, there is an unphysically high activation energy (10.8 eV) for 3/4-grain-junction-controlled boundary migration that suggests more and more grain junctions become frozen at lower and lower temperature, so the few remaining mobile boundaries will also become immobile if there are pores to pin them. Therefore, it is advantageous to choose a T_2 as low as feasible, which is 100 °C below T_{tr} (1300 °C) in our 8YSZ study. On the other hand, once pores are all gone, the few remaining mobile boundaries can start migrating. Therefore, further prolong annealing will cause localized grain growth/shrinkage, which broadens the grain-size distribution. Again, a lower T_2 is advisable as it leaves a wider time window to terminate heating before microstructure begins deteriorating. (In 8YSZ, it takes 500–1000 h at ≤ 1200 °C for deterioration to become evident.^[42]) Completely frozen microstructure was found in this work and in the literature for Al_2O_3 ,^[15] BaTiO_3 ,^[17] Y_2O_3 ,^[53] and $\text{Ni}_{0.2}\text{Cu}_{0.2}\text{Zn}_{0.6}\text{Fe}_2\text{O}_4$ ^[17] in T_2 -sintering for up to 40 h, which is enough to reach full density and is a comparable schedule used in industry, for example, for MLCC.

6. Conclusions

In summary, new theoretical and statistical analysis of microstructure evolution during sintering has revealed a sweet spot at an intermediate density that enables highly uniform bulk, dense nanomaterials to obtain for ceramics and powder-metallurgy metals alike, and it also explains why materials of superior reliability often arise from two-step sintering. This was expressly demonstrated for a dense bulk nanocrystalline Al_2O_3 , a ceramic known to be difficult to sinter without sintering additives, yet the achieved grain-size uniformity exceeded the theoretical “limit” predicted by Hillert 60 years ago. The success will encourage the development of other highly uniform nanocrystalline materials for structural and functional applications.

7. Experimental Section

$\alpha\text{-Al}_2\text{O}_3$ powders were prepared by high-energy ball milling followed by corrosion and separation.^[61] $\alpha\text{-Al}_2\text{O}_3$ powders with varying sizes and purities (see Table S2, Supporting Information for details) were obtained by adjusting the pH during the separation process. Pressed pellets of $\alpha\text{-Al}_2\text{O}_3$ powders were heated in air at 10 °C min^{-1} to various temperatures, then either held there for a certain holding time or immediately cooled as specified in Supporting Information. Two-step sintering was conducted by firstly heating the pellet at 10 °C min^{-1} to T_1 , then, without holding, immediately cooling it at 5 °C min^{-1} to T_2 , and held there for 20–40 h. The theoretical density of Al_2O_3 was chosen as 3.96 g cm^{-3} . Fractured fragments of sintered pellets which underwent intergranular fracture were examined under a transmission electron microscope (TEM; FEI Tecnai G2 F30). Relatively flat fractured and thermally etched (at 50 °C lower than sintering temperature for 0.5 h) surfaces of the pellets were examined under scanning electron microscope (SEM; Tescan LYRA3 XMU).

Pressed pellets of 8YSZ powders (TZ-8Y, Tosoh Co., Tokyo, Japan) were heated in air to 1280 °C without holding to obtain porous sample, or to 1300 °C and held there for 12 h to obtain dense sample, both with 5 °C min^{-1} heating/cooling rate. Pressed pellets of 3YSZ powders (TZ-3Y-E, Tosoh Co., Tokyo, Japan) were heated in air to 1240 °C without holding to obtain porous sample, or to 1300 °C and held there for 12 h to obtain dense sample, both with 5 °C min^{-1} heating/cooling rate. The theoretical density of 8YSZ/3YSZ was chosen as 6.08 g cm^{-3} . Polished and thermally etched (1220 °C for 0.2 h for porous/dense 8YSZ and dense 3YSZ, 1150 °C for 0.2 h for porous 3YSZ) surfaces were examined under SEM (Quanta 600, FEI Co.).

Mo powders were prepared via a solution combustion method^[62] followed by hydrogen reduction, using ammonium molybdate hydrate $(\text{NH}_4)_6\text{Mo}_7\text{O}_{24}\cdot 4\text{H}_2\text{O}$ as a precursor. Pressed pellets of Mo powders were sintered in a hydrogen atmosphere with 10 °C min^{-1} heating rate and 5 °C min^{-1} cooling rate. Normal sintering was conducted at 1400 °C for 2 h. Two-step sintering was conducted by first heating the pellet to 1180 °C and held for 1 h, then cooling it to 1100 °C and held there for 10 h. The theoretical density of Mo was chosen as 10.2 g cm^{-3} . Relatively flat fractured surfaces of the pellets, which underwent intergranular fracture, were examined under SEM (Hitachi UHR SU8100).

90W-10Re powders were prepared via a similar solution combustion method followed by hydrogen reduction, using ammonium metatungstate hydrate $(\text{NH}_4)_6\text{H}_2\text{W}_{12}\text{O}_{40}\cdot x\text{H}_2\text{O}$ and ammonium perchlorate NH_4ReO_4 as precursors with a weight ratio of W:Re = 9:1. Pressed pellets of 90W-10Re powders were sintered in a hydrogen atmosphere with 10 °C min^{-1} heating rate and 5 °C min^{-1} cooling rate. Normal sintering was conducted at 1500 °C for 2 h. Two-step sintering was conducted by first heating the pellet to 1200 °C and held for 1 h, then cooling it to 1100 °C and held there for 20 h. The theoretical density of 90W-10Re was chosen as 19.4 g cm^{-3} . Relatively flat fractured surfaces of the pellets, which underwent intergranular fracture, were examined under SEM (FEI Quanta FEG 450).

The BT samples analyzed were from a previous study.^[4] As described therein, powders were prepared by a precipitation/coating method on commercial BaTiO_3 powders (KCM Co. Ltd., Nagoya, Japan). Pressed pellets were sintered in a reducing atmosphere ($\text{H}_2\text{—N}_2\text{—H}_2\text{O}$ gas mixture, oxygen partial pressure $10^{-13}\text{—}10^{-15}\text{ Pa}$) with heating schedules described in Figure 1 of ref. [4]. The theoretical density of BT was chosen as 6.02 g cm^{-3} . Surfaces of the pellets were examined under SEM (MERLIN VP Compact, Carl Zeiss Corp.).

The BT-BZNT samples analyzed were from another previous study.^[57] As described therein, powders were prepared by a solid-state synthesis method, and their green body tapes for multilayer capacitors were prepared by a tape casting method. Normal sintering was conducted at 1150 °C for 3 h. Two-step sintering was conducted by firstly heating the pellet to 1190 °C and held for 1 min, then cooling it to 1040 °C and held there for 3 h. Surfaces of the sintered pieces were examined under SEM (Supra 40/40vp, Carl Zeiss Corp.).

Average grain sizes and grain size distributions were calculated by measuring the maximum diameter (i.e., along the direction that gives the largest diameter) for N grains (N typically in the range of 300–600; see Table S1–S3, Supporting Information for more details).

Supporting Information

Supporting Information is available from the Wiley Online Library or from the author.

Acknowledgements

I.-W.C. and Y.D. acknowledge the support by the Department of Energy (BES grant no. DEFG02-11ER46814) and the LRSM facilities funded by the U.S. National Science Foundation (grant no. DMR-1120901) during Y.D.'s PhD research at the University of Pennsylvania that initiated the present work. Ju L., Y.D., and D.D. acknowledge the support by the U.S. Department of Energy (USDOE), Office of Energy Efficiency and Renewable Energy (EERE), Advanced Manufacturing Office (AMO) R&D Projects Emerging Research Exploration, under DOE Idaho Operations Office with contract no. DE-AC07-05ID14517. Jiangong L. and H.Y. acknowledge the support by the National Natural Science Foundation of China (51772137) and the Fundamental Research Funds for the Central Universities (lzujbky-2019-sp03). L.Z. acknowledges National Key Research and Development Program of China (grant no. 2017YFB0305600). X.W. acknowledges the support by the National Key Research and Development Program of China (grant no. 2017YFB0406302) and the Key Area Research Plan of Guangdong (grant no. 2019B010937001).

Conflict of Interest

The authors declare no conflict of interest.

Keywords

ceramics, grain growth, microstructure, nanocrystalline materials, refractory metals, sintering

Received: September 11, 2020
Published online:

- [1] T. Chookajorn, H. A. Murdoch, C. A. Schuh, *Nature* **2012**, 337, 951.
- [2] J. F. Curry, T. F. Babuska, T. A. Furnish, P. Lu, D. P. Adams, A. B. Kustas, B. L. Nation, M. T. Dugger, M. Chandross, B. G. Clark, B. L. Boyce, C. A. Schuh, N. Argibay, *Adv. Mater.* **2018**, 30, 1802026.
- [3] X. Zhou, X. Y. Li, K. Lu, *Science* **2018**, 360, 526.
- [4] Q. Zhao, H. Gong, X. Wang, I. W. Chen, L. Li, *J. Am. Ceram. Soc.* **2016**, 99, 191.
- [5] A. G. Evans, *J. Am. Ceram. Soc.* **1982**, 65, 127.
- [6] M. Hillert, A. Metal, **1965**, 13, 227.
- [7] I. M. Lifshitz, V. V. Slyozov, *J. Phys. Chem. Solids* **1961**, 19, 35.
- [8] C. Z. Wagner, *Berichte der Bunsengesellschaft für Physikalische Chemie* **1961**, 65, 581.
- [9] Y. Dong, I. W. Chen, arXiv **2017**, <https://arxiv.org/abs/1708.04092>.
- [10] L. A. Xue, I. W. Chen, *J. Am. Ceram. Soc.* **1990**, 73, 3518.
- [11] S. J. Dillon, M. P. Harmer, *J. Am. Ceram. Soc.* **2008**, 91, 2304.
- [12] S. J. Dillon, M. P. Harmer, *J. Am. Ceram. Soc.* **2008**, 91, 2314.
- [13] B.-N. Kim, K. Hiraga, K. Morita, H. Yoshida, S. Mater, **2007**, 57, 607.
- [14] F. J. T. Lin, L. C. De Jonghe, M. N. Rahaman, *J. Am. Ceram. Soc.* **1997**, 80, 2269.
- [15] R. Guo, W. Cao, X. Mao, J. Li, *J. Am. Ceram. Soc.* **2016**, 99, 3556.
- [16] W. Cao, X. Mao, Y. Yuan, L. Li, L. Zhao, J. Li, *J. Eur. Ceram. Soc.* **2017**, 37, 4005.
- [17] X. Wang, X. Deng, H. Bai, H. Zhou, W. Qu, L. Li, I. W. Chen, *J. Am. Ceram. Soc.* **2006**, 89, 438.
- [18] S. Wang, L. Zhang, K. Brinkman, F. Chen, *Electrochem. Acta* **2013**, 87, 194.
- [19] X. Zhou, L. Liu, J. Zhen, S. Zhu, B. Li, K. Sun, P. Wang, *J. Power Sources* **2011**, 196, 5000.
- [20] P. L. Chen, I. W. Chen, *J. Am. Ceram. Soc.* **1996**, 79, 1793.
- [21] Y. Dong, H. Wang, I. W. Chen, *J. Am. Ceram. Soc.* **2017**, 100, 876.
- [22] V. Esposito, D. W. Ni, Z. He, W. Zhang, A. S. Prasad, J. A. Glasscock, C. Chatzichristodoulou, S. Ramousse, A. Kaiser, *Acta Mater.* **2013**, 61, 6290.
- [23] F. Rubio-Marcos, P. Ochoa, J. F. Fernandez, *J. Eur. Ceram. Soc.* **2007**, 27, 4125.
- [24] C.-L. Tsai, V. Roddatis, C. V. Chandran, Q. Ma, S. Uhlenbruck, M. Bram, P. Heitjans, O. Guillon, *ACS Appl. Mater. Interfaces* **2016**, 8, 10617.
- [25] A. Sharafi, C. G. Haslam, R. D. Kerns, J. Wolfenstine, J. Sakamoto, *J. Mater. Chem. A* **2017**, 5, 21491.
- [26] D. Marrero-Lopez, J. C. Ruiz-Morales, J. Pena-Martinez, M. C. Martin-Sedeno, J. R. Ramos-Barrado, *Solid State Ionics* **2011**, 186, 44.
- [27] S. Yu, H. Bi, J. Sun, L. Zhu, H. Yu, C. Lu, X. Liu, *J. Alloy Compd.* **2019**, 777, 244.
- [28] B. Rambabu, S. Ghosh, W. Zhao, H. Jena, *J. Power Sources* **2006**, 159, 21.
- [29] L. An, A. Ito, T. Goto, *J. Eur. Ceram. Soc.* **2012**, 32, 3097.
- [30] D. Ehre, R. Chaim, *J. Mater. Sci.* **2008**, 43, 6139.
- [31] M. Sokol, M. Halabi, S. Kalabukhov, N. Frage, *J. Eur. Ceram. Soc.* **2017**, 37, 755.
- [32] H. Shimizu, K. Kobayashi, Y. Mizuno, C. A. Randall, *J. Am. Ceram. Soc.* **2014**, 97, 1791.
- [33] G. H. Haertling, in *Ceramic Materials for Electronics* (Eds: R. C. Buchanan, M. Dekker), CRC Press, New York **1991**, pp. 139–225.
- [34] Y. Yoshikawa, K. Tsuzuki, *J. Am. Ceram. Soc.* **1992**, 75, 2520.
- [35] W. Rheinheimer, M. J. Hoffmann, *J. Mater. Sci.* **2016**, 51, 1756.
- [36] M. Mazaheri, Z. R. Hesabi, S. K. Sadrnezhad, S. Mater, **2008**, 59, 139.
- [37] X. Li, L. Zhang, Y. Dong, R. Gao, M. Qin, X. Qu, *Acta Mater* **2020**, 186, 116.
- [38] P. L. Chen, I. W. Chen, *J. Am. Ceram. Soc.* **1996**, 79, 1801.
- [39] R. Chaim, M. Kalina, J. Z. Shen, *J. Eur. Ceram. Soc.* **2017**, 27, 3331.
- [40] A. Ikesue, *Opt. Mater.* **2002**, 19, 183.
- [41] A. E. Paladino, E. A. Maguire, *J. Am. Ceram. Soc.* **1970**, 53, 98.
- [42] E. Savary, S. Marinell, H. Colder, C. Harnois, F. X. Lefevre, R. Retoux, *Powder Tech.* **2011**, 208, 521.
- [43] M. Mazaheri, A. Simchi, F. Golestani-Fard, *J. Eur. Ceram. Soc.* **2008**, 28, 2933.
- [44] M. Mazaheri, M. Valefi, Z. R. Hesabi, S. K. Sadrnezhad, *Ceram. Int.* **2009**, 35, 13.
- [45] Y. Dong, I. W. Chen, *J. Am. Ceram. Soc.* **2018**, 101, 1857.
- [46] C. B. Murray, D. J. Norris, M. G. Bawendi, *J. Am. Chem. Soc.* **1993**, 115, 8706.
- [47] P. W. Voorhees, *J. Stat. Phys.* **1985**, 38, 231.
- [48] W. D. Kingery, H. K. Bowen, D. R. Uhlmann, *Introduction to Ceramics*, 2nd ed., John Wiley and Sons, Hoboken, NJ **1976**, pp. 454–455.
- [49] G. N. Hassold, I. W. Chen, D. J. Srolovitz, *J. Am. Ceram. Soc.* **1990**, 73, 2857.
- [50] I. W. Chen, G. N. Hassold, D. J. Srolovitz, *J. Am. Ceram. Soc.* **1990**, 73, 2865.

- [51] I. W. Chen, L. A. Xue, *J. Am. Ceram. Soc.* **1990**, 73, 2585.
- [52] I. W. Chen, X. H. Wang, *Nature* **2000**, 404, 168.
- [53] X. H. Wang, P. L. Chen, I. W. Chen, *J. Am. Ceram. Soc.* **2006**, 89, 431.
- [54] Y. I. Lee, Y. W. Kim, M. Mitomo, D. Y. Kim, *J. Am. Ceram. Soc.* **2003**, 86, 1803.
- [55] H. Jiang, X. Wang, W. Lei, G. Fan, W. Lu, *J. Eur. Ceram. Soc.* **2019**, 39, 249.
- [56] H. Yang, L. Li, W. Cao, Y. Liu, M. Mukhtar, L. Zhao, Y. Kang, Y. Dong, J. Li, *J. Eur. Ceram. Soc.* **2020**, 40, 1505.
- [57] P. Zhao, H. Wang, L. Wu, L. Chen, Z. Cai, L. Li, X. Wang, *Adv. Energy Mater.* **2019**, 9, 1803048.
- [58] P.-L. Chen, I. W. Chen, *J. Am. Ceram. Soc.* **1996**, 79, 3129.
- [59] P.-L. Chen, I. W. Chen, *J. Am. Ceram. Soc.* **1997**, 80, 637.
- [60] C. A. Handwerker, J. M. Dynys, R. M. Cannon, R. L. Coble, *J. Am. Ceram. Soc.* **1990**, 73, 1371.
- [61] L. Li, S. Pu, Y. Liu, L. Zhao, J. Ma, J. Li, *Adv. Powder Tech.* **2018**, 29, 2194.
- [62] M. Qin, Z. Chen, P. Chen, S. Zhao, R. Li, J. Ma, X. Qu, *Int. J. Refract. Met. Hard Mater.* **2017**, 68, 145.



Supporting Information

for *Adv. Funct. Mater.*, DOI: 10.1002/adfm.202007750

Ultra-Uniform Nanocrystalline Materials via Two-Step Sintering

Yanhao Dong, Hongbing Yang, Lin Zhang, Xingyu Li, Dong Ding, Xiaohui Wang, Ju Li, Jiangong Li,* and I-Wei Chen**

Supporting Information

Ultra-Uniform Nanocrystalline Materials via Two-Step Sintering

Yanhao Dong¹, Hongbing Yang², Lin Zhang³, Xingyu Li³, Dong Ding⁴, Xiaohui Wang⁵, Ju Li^{1,6,*}, Jiangong Li^{2,*}, I-Wei Chen^{7,*}

¹Department of Nuclear Science and Engineering, Massachusetts Institute of Technology, Cambridge, MA 02139, USA

²Institute of Materials Science and Engineering and MOE Key Laboratory for Special Functional Materials and Structure Design, Lanzhou University, Lanzhou 730000, China

³Beijing Advanced Innovation Center for Materials Genome Engineering, Institute for Advanced Materials and Technology, University of Science and Technology Beijing, Beijing 100083, China

⁴Energy & Environmental Science and Technology, Idaho National Laboratory, Idaho Falls, ID 83415, USA

⁵State Key Laboratory of New Ceramics and Fine Processing, School of Materials Science and Engineering, Tsinghua University, Beijing 100084, China

⁶Department of Materials Science and Engineering, Massachusetts Institute of Technology, Cambridge, MA 02139, USA

⁷Department of Materials Science and Engineering, University of Pennsylvania, Philadelphia, PA 19104, USA

Table of content

Supplementary Figures S1-S4	Page 2-5
Supplementary Table S1-S3	Page 6-9

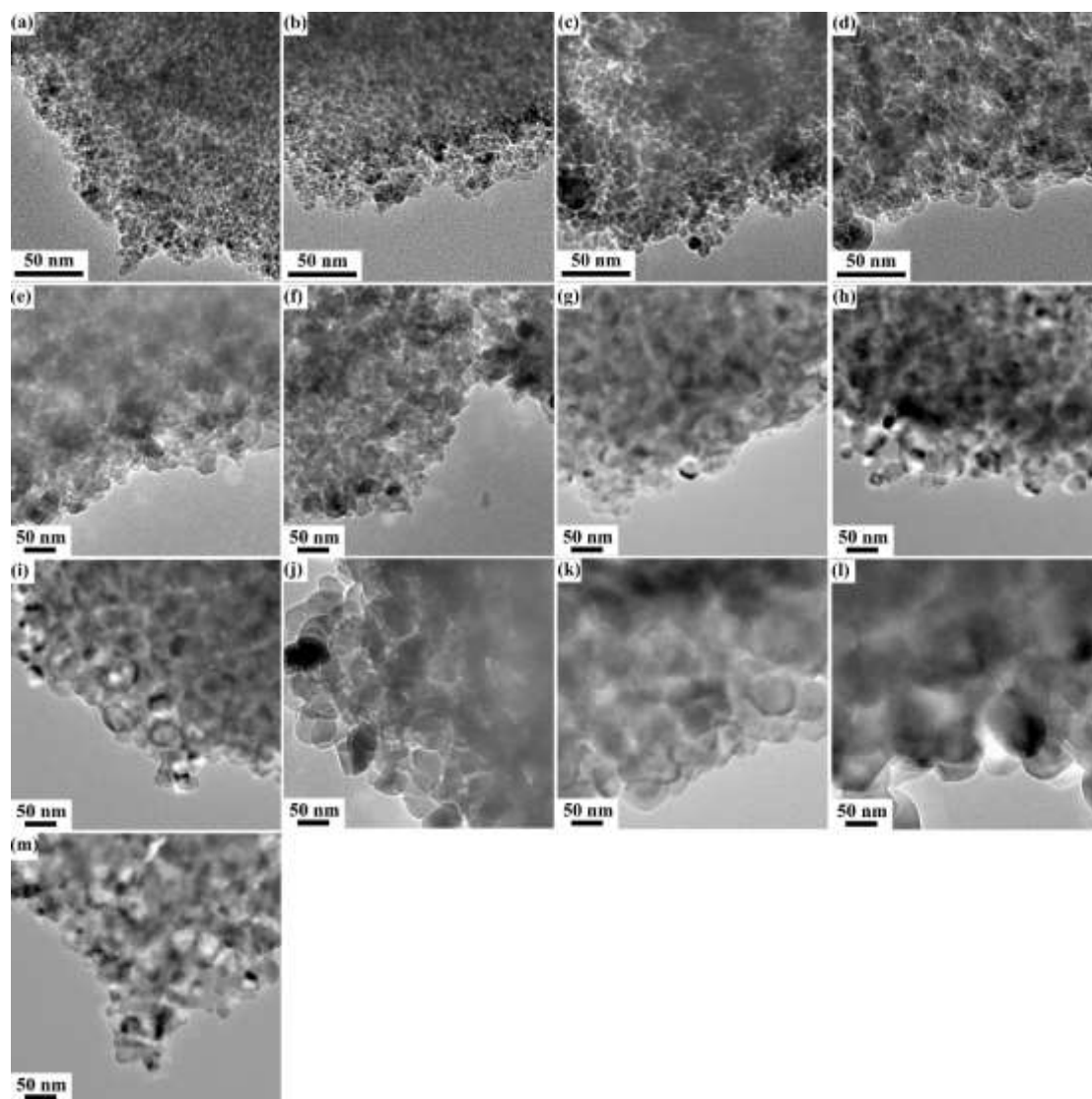


Figure S1 TEM images of Al_2O_3 heated to (a) 700°C, (b) 800°C, (c) 900°C, (d) 1000°C, (e) 1050°C, (f) 1100°C, (g) 1125°C, (h) 1150°C, (i) 1175°C, (j) 1200°C, (k) 1250°C, and (l) 1300°C, all without holding. (m) Two-step sintered Al_2O_3 at 1150°C (T_1) without holding and then at 1025°C (T_2) for 40 h.

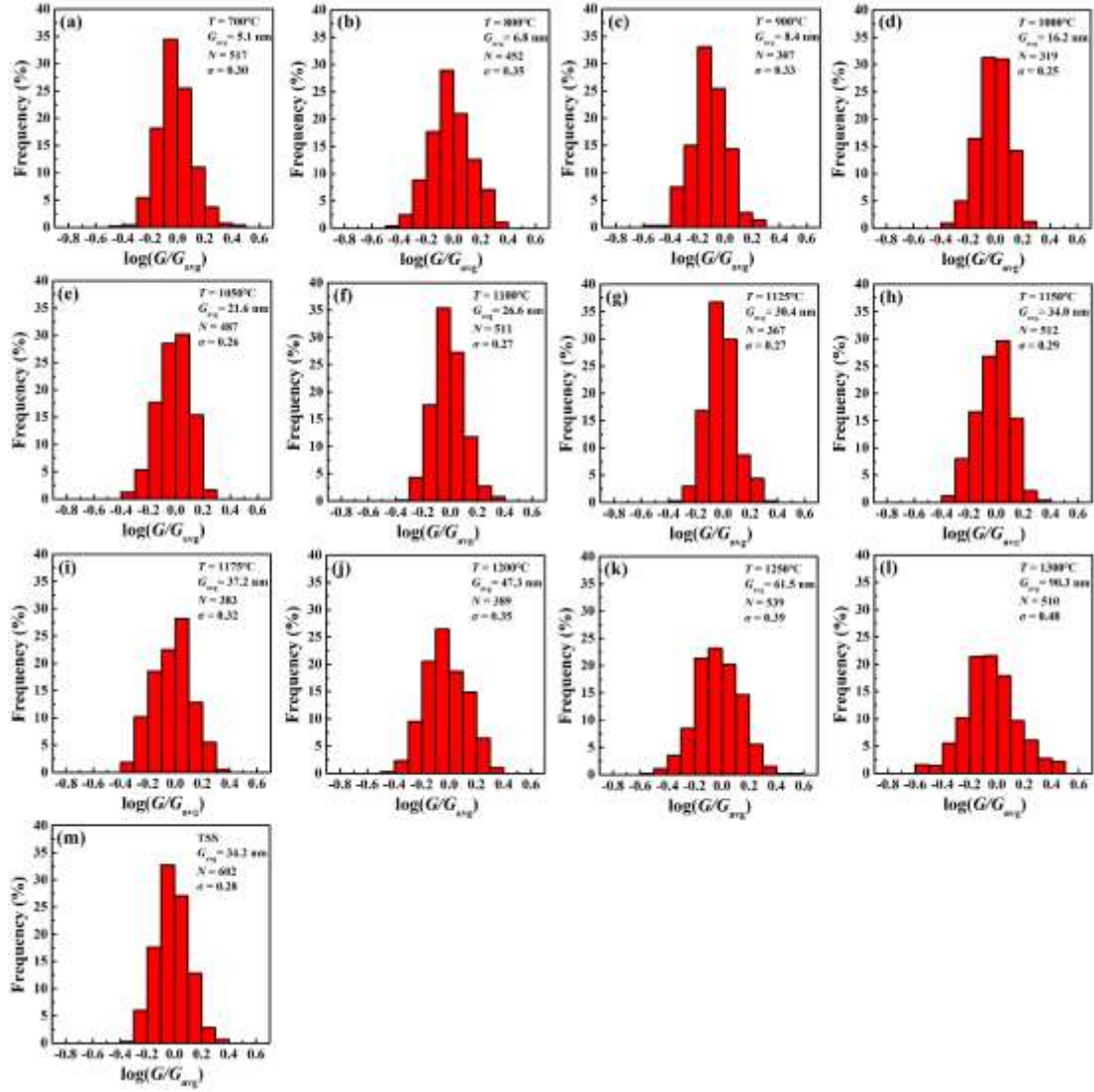


Figure S2 Normalized grain size distribution measured from TEM images in **Fig. S1**.

Also listed are G_{avg} , number N of measured grains and σ . Al_2O_3 samples were sintered at (a) 700°C, (b) 800°C, (c) 900°C, (d) 1000°C, (e) 1050°C, (f) 1100°C, (g) 1125°C, (h) 1150°C, (i) 1175°C, (j) 1200°C, (k) 1250°C, and (l) 1300°C, all without holding. (m) Two-step sintered Al_2O_3 at 1150°C (T_1) without holding and then at 1025°C (T_2) for 40 h.

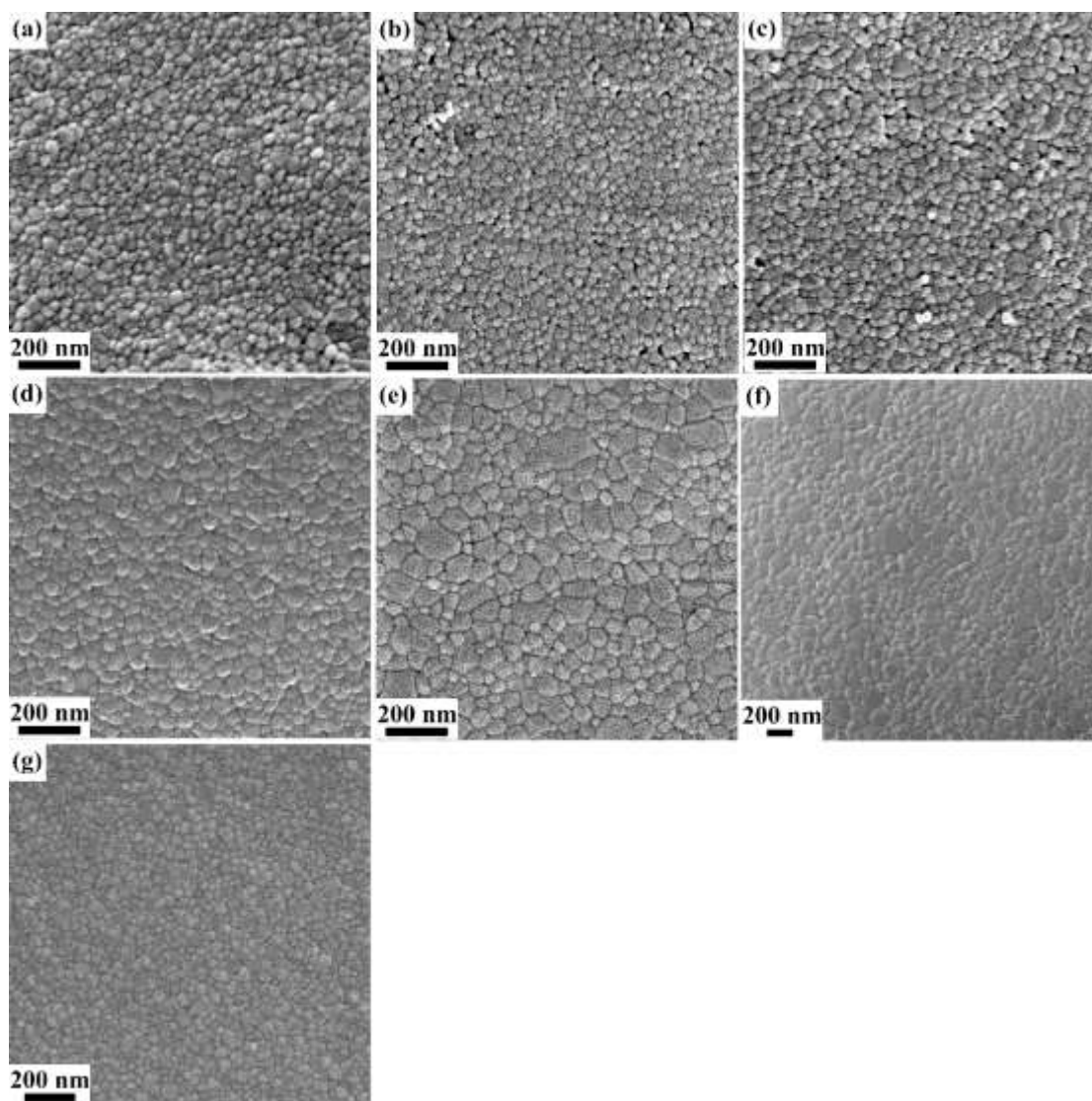


Figure S3 SEM images of Al_2O_3 sintered at (a) 1125°C, (b) 1150°C, (c) 1175°C, (d) 1200°C, (e) 1250°C, and (f) 1300°C, all without holding. (g) Two-step sintered Al_2O_3 at 1150°C (T_1) without holding and then at 1025°C (T_2) for 40 h.

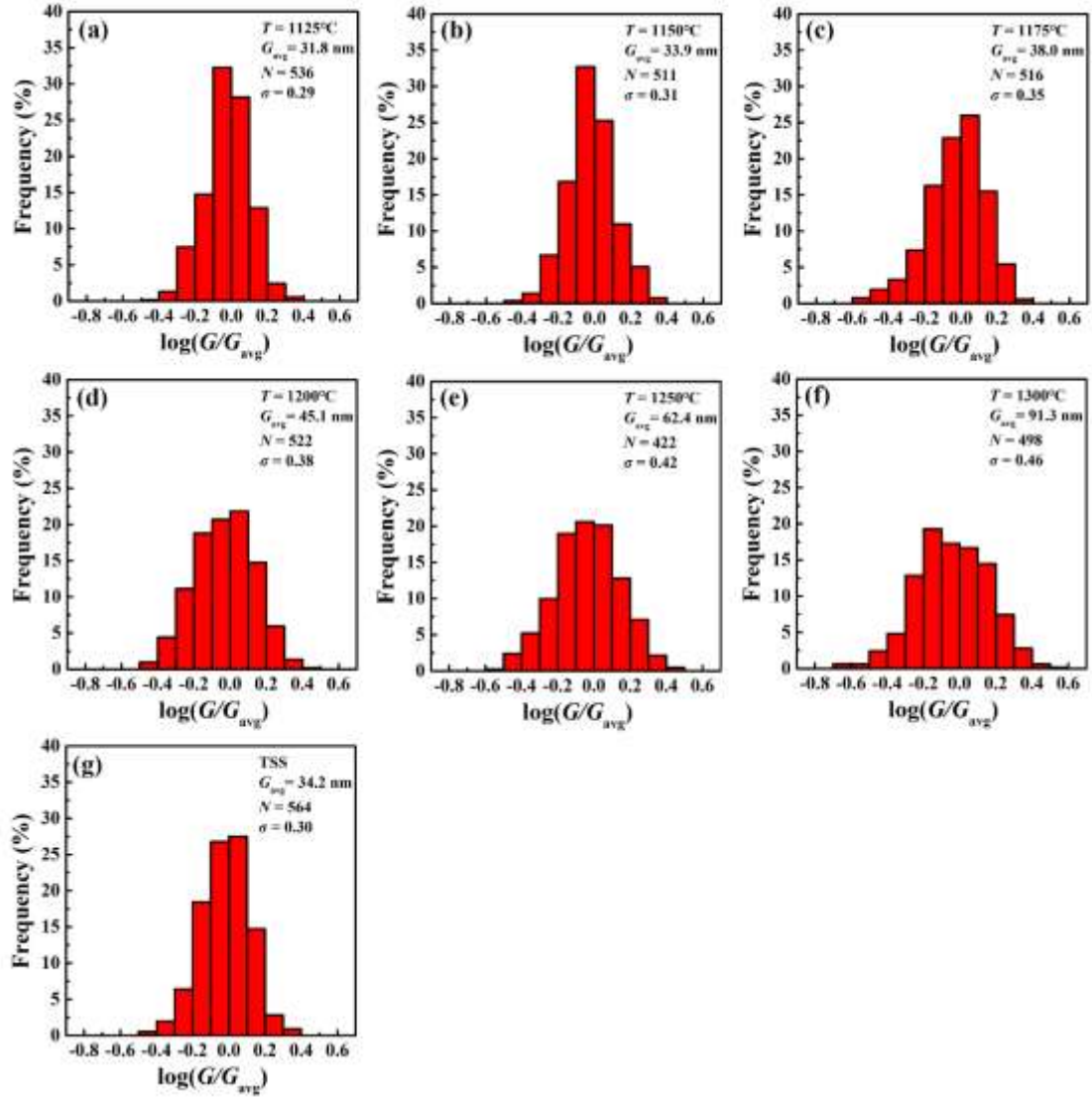


Figure S4 Normalized grain size distribution measured from SEM images in **Fig. S3**. Also listed are G_{avg} , number N of measured grains and σ . Al_2O_3 samples were sintered at (a) 1125°C , (b) 1150°C , (c) 1175°C , (d) 1200°C , (e) 1250°C , and (f) 1300°C , all without holding. (g) Two-step sintered Al_2O_3 at 1150°C (T_1) without holding and then at 1025°C (T_2) for 40 h.

Table S1 Measured G_{avg} , N and σ for dense polycrystalline materials. Materials processed by two-step sintering in red, and by other techniques in blue.

Materials	Symbol	G_{avg}	N	σ	Reference
Al_2O_3	Filled star	385nm	431	0.57	This work
Al_2O_3	Filled square	0.33 μm	209	0.50	Fig. 2a, Ref. 10
Al_2O_3	Filled square	4.0 μm	261	0.69	Fig. 3a, Ref. 11
Al_2O_3	Filled square	4.4 μm	421	0.39	Fig.1a, Ref. 12
Al_2O_3	Filled square	31.4 μm	510	0.65	Fig.1d, Ref. 12
Al_2O_3	Filled square	0.24 μm	148	0.46	Fig.3, Ref. 13
Al_2O_3	Filled square	1.1 μm	216	0.48	Fig.8b, Ref. 14
Al_2O_3	Filled star	34nm	564	0.30	This work
Al_2O_3	Filled square	70nm	343	0.36	This work
Al_2O_3	Filled square	164nm	468	0.39	This work
Al_2O_3	Filled square	55nm	525	0.34	Fig. 6, Ref. 15
Al_2O_3	Filled square	41nm	536	0.36	Fig. 7a, Ref. 16
Al_2O_3	Filled square	32nm	612	0.34	Fig. 7b, Ref. 16
Al_2O_3	Filled square	54nm	530	0.34	Fig. 7c, Ref. 16
BaTiO_3	Open square	0.19 μm	459	0.47	This work
BaTiO_3	Open square	0.16 μm	129	0.48	Fig. 2b, Ref. 4
BaTiO_3	Open square	1.2 μm	223	0.37	Fig. 4f, Ref. 17
BaTiO_3	Open square	0.18 μm	514	0.36	This work
BaTiO_3	Open square	0.16 μm	127	0.44	Fig. 2d, Ref. 4
BaTiO_3	Open square	68nm	532	0.37	Fig. 4b, Ref. 17
BaTiO_3	Open square	98nm	357	0.42	Fig. 4c, Ref. 17
BaTiO_3	Open square	0.20 μm	521	0.38	Fig. 4d, Ref. 17
BT-BZNT	Open square	0.66 μm	401	0.60	This work
BT-BZNT	Open square	0.52 μm	535	0.48	This work
$\text{BaZr}_{0.1}\text{Ce}_{0.7}\text{Y}_{0.1}\text{Yb}_{0.1}\text{O}_{3-x}$	Half-filled square	0.49 μm	98	0.40	Fig.3a, Ref. 18
$\text{BaZr}_{0.1}\text{Ce}_{0.7}\text{Y}_{0.1}\text{Yb}_{0.1}\text{O}_{3-x}$	Half-filled square	0.57 μm	80	0.40	Fig.3b, Ref. 18

$\text{BaZr}_{0.1}\text{Ce}_{0.7}\text{Y}_{0.1}\text{Yb}_{0.1}\text{O}_{3-x}$	Half-filled square	$0.30\mu\text{m}$	229	0.36	Fig.3c, Ref. 18
$\text{BaZr}_{0.1}\text{Ce}_{0.7}\text{Y}_{0.1}\text{Yb}_{0.1}\text{O}_{3-x}$	Half-filled square	$1.3\mu\text{m}$	486	0.36	Fig.5a, Ref. 19
$\text{BaZr}_{0.1}\text{Ce}_{0.7}\text{Y}_{0.1}\text{Yb}_{0.1}\text{O}_{3-x}$	Half-filled square	$2.3\mu\text{m}$	176	0.39	Fig.5b, Ref. 19
CeO_2	Filled cycle	$0.67\mu\text{m}$	115	0.49	Fig. 2a, Ref. 20
CeO_2	Filled cycle	$0.39\mu\text{m}$	119	0.44	Fig. 2b, Ref. 20
CeO_2	Filled cycle	$16.6\mu\text{m}$	93	0.52	Fig. 2c, Ref. 20
CeO_2	Filled cycle	$0.54\mu\text{m}$	76	0.42	Fig. 2d, Ref. 20
CeO_2	Filled cycle	$20.9\mu\text{m}$	74	0.43	Fig. 2e, Ref. 20
$\text{Gd}_{0.1}\text{Ce}_{0.9}\text{O}_{1.95}$	Open cycle	$0.51\mu\text{m}$	237	0.43	Fig.1c, Ref. 21
$\text{Gd}_{0.1}\text{Ce}_{0.9}\text{O}_{1.95}$	Open cycle	$0.77\mu\text{m}$	231	0.38	Fig.5b, Ref. 22
$(\text{K},\text{Na},\text{Li})(\text{Nb},\text{Ta},\text{Sb})\text{O}_3$	Half-filled cycle	$1.6\mu\text{m}$	190	0.60	Fig.5d, Ref. 23
$\text{Li}_7\text{La}_3\text{Zr}_2\text{O}_{12}$	Filled triangle	$5.4\mu\text{m}$	426	0.49	Fig.1b, Ref. 24
$\text{Li}_7\text{La}_3\text{Zr}_2\text{O}_{12}$	Filled triangle	$2.2\mu\text{m}$	332	0.41	Fig.3a, Ref. 25
$\text{Li}_7\text{La}_3\text{Zr}_2\text{O}_{12}$	Filled triangle	$29.1\mu\text{m}$	233	0.47	Fig.3b, Ref. 25
$\text{Li}_7\text{La}_3\text{Zr}_2\text{O}_{12}$	Filled triangle	$39.2\mu\text{m}$	144	0.46	Fig.3c, Ref. 25
$\text{Li}_7\text{La}_3\text{Zr}_2\text{O}_{12}$	Filled triangle	$37.6\mu\text{m}$	150	0.47	Fig.3d, Ref. 25
$(\text{La},\text{Sr})(\text{Ga},\text{Mg})\text{O}_3$	Open triangle	$1.8\mu\text{m}$	121	0.46	Fig.1c, Ref. 26
$(\text{La},\text{Sr})(\text{Ga},\text{Mg})\text{O}_3$	Open triangle	$2.2\mu\text{m}$	131	0.42	Fig.1d, Ref. 26
$(\text{La},\text{Sr})(\text{Ga},\text{Mg})\text{O}_3$	Open triangle	$2.0\mu\text{m}$	161	0.36	Fig.2a, Ref. 27
$(\text{La},\text{Sr})(\text{Ga},\text{Mg})\text{O}_3$	Open triangle	$3.4\mu\text{m}$	260	0.39	Fig.6c, Ref. 28
$(\text{La},\text{Sr})(\text{Ga},\text{Mg})\text{O}_3$	Open triangle	$5.0\mu\text{m}$	139	0.37	Fig.6d, Ref. 28
$\text{Lu}_3\text{Al}_5\text{O}_{12}$	Half-filled triangle	$0.39\mu\text{m}$	218	0.38	Fig.3a, Ref. 29
MgO	Filled diamond	72nm	212	0.43	Fig.1a, Ref. 30
MgAl_2O_4	Open diamond	93nm	145	0.40	Fig.3c, Ref. 31
MgAl_2O_4	Open diamond	85nm	171	0.45	Fig.3d, Ref. 31
Mo	Filled pentagon	$0.89\mu\text{m}$	322	0.49	This work
Mo	Filled pentagon	$0.37\mu\text{m}$	259	0.38	This work
NaNbO_3	Half-filled diamond	$4.8\mu\text{m}$	156	0.36	Fig.4a, Ref. 32
$(\text{Pb},\text{La})(\text{Zr},\text{Ti})\text{O}_3$	Filled hexagon	$3.2\mu\text{m}$	532	0.48	Fig. 16, Ref. 33

(Pb,La)(Zr,Ti)O ₃	Filled hexagon	1.2μm	111	0.44	Fig.18, Ref. 34
SrTiO ₃	Open hexagon	5.8μm	421	0.68	Fig. 3a, Ref. 35
SrTiO ₃	Open hexagon	4.3μm	457	0.96	Fig. 3b, Ref. 35
SrTiO ₃	Open hexagon	3.3μm	445	0.81	Fig. 3c, Ref. 35
SrTiO ₃	Open hexagon	14.0μm	506	0.60	Fig. 3d, Ref. 35
SrTiO ₃	Open hexagon	2.6μm	462	0.78	Fig. 5a, Ref. 35
SrTiO ₃	Open hexagon	3.6μm	422	0.84	Fig. 5b, Ref. 35
SrTiO ₃	Open hexagon	5.1μm	470	0.98	Fig. 5c, Ref. 35
SrTiO ₃	Open hexagon	2.2μm	519	0.69	Fig. 7a, Ref. 35
SrTiO ₃	Open hexagon	3.1μm	545	0.75	Fig. 7b, Ref. 35
SrTiO ₃	Open hexagon	3.8μm	440	0.86	Fig. 7c, Ref. 35
TiO ₂	Half-filled hexagon	0.13μm	371	0.40	Fig. 6, Ref. 36
W	Filled pentagon	1.8μm	371	0.54	Fig. 5a, Ref. 37
W	Filled pentagon	0.83μm	549	0.41	Fig. 5b, Ref. 37
90W-10Re	Filled pentagon	2.2μm	253	0.44	This work
90W-10Re	Filled pentagon	0.33μm	305	0.35	This work
Y ₂ O ₃	Open pentagon	4.1μm	54	0.42	Fig. 3b, Ref. 38
Y ₂ O ₃	Open pentagon	0.73μm	85	0.40	Fig. 3c, Ref. 38
Y ₂ O ₃	Open pentagon	0.23μm	98	0.42	Fig. 3d, Ref. 38
Y ₂ O ₃	Open pentagon	0.31μm	70	0.45	Fig. 3e, Ref. 38
Y ₃ Al ₅ O ₁₂	Half-filled pentagon	0.42μm	71	0.46	Fig.8a, Ref. 39
Y ₃ Al ₅ O ₁₂	Half-filled pentagon	24.5μm	431	0.44	Fig.1, Ref. 40
Y ₃ Fe ₅ O ₁₂	Open star	5.1μm	235	0.38	Fig.5a, Ref. 41
ZnO	Half-filled star	0.34μm	469	0.37	Fig.7b, Ref. 42
3 mol% Y ₂ O ₃ -ZrO ₂	Plus	178nm	529	0.39	This work
3 mol% Y ₂ O ₃ -ZrO ₂	Plus	78nm	521	0.32	Fig. 6a, Ref. 43
3 mol% Y ₂ O ₃ -ZrO ₂	Plus	0.21μm	130	0.39	Fig. 6b, Ref. 43
3 mol% Y ₂ O ₃ -ZrO ₂	Plus	88nm	469	0.43	Fig. 6c, Ref. 43
8 mol% Y ₂ O ₃ -ZrO ₂	Cross	1.19μm	354	0.53	This work

8 mol% Y ₂ O ₃ -ZrO ₂	Cross	0.27μm	427	0.34	Fig. 9b, Ref. 44
8 mol% Y ₂ O ₃ -ZrO ₂	Cross	0.34μm	523	0.41	Fig. 2c, Ref. 45

Table S2 Measured G_{avg} , N and σ for three different α -Al₂O₃ powders and their two-step sintered ceramics of density ρ .

α -Al ₂ O ₃ powders				Two-step sintered dense Al ₂ O ₃				
Purity (wt%)	G_{avg} (nm)	N	σ	Sintering condition	ρ (%)	G_{avg} (nm)	N	σ
99.958	4.7	1018	0.23	$T_1=1150^\circ\text{C}$ for 0 h, $T_2=1025^\circ\text{C}$ for 40 h	99.6	34	564	0.30
99.938	11.6	675	0.41	$T_1=1200^\circ\text{C}$ for 0 h, $T_2=1000^\circ\text{C}$ for 20 h	99.1	70	343	0.36
99.914	16.1	526	0.43	$T_1=1275^\circ\text{C}$ for 0 h, $T_2=1075^\circ\text{C}$ for 20 h	98.9	164	468	0.39

Table S3 Measured ρ , G_{avg} , N and σ for Mo, 90W-10Re, BT and BT-BZNT via two-step sintering and one-step sintering.

Materials	Sintering condition	ρ (%)	G_{avg} (μm)	N	σ
Mo	$T_1=1180^\circ\text{C}$ for 1 h, $T_2=1110^\circ\text{C}$ for 10 h	98.8	0.37	259	0.38
	1400°C for 3 h	97.8	0.89	322	0.49
90W-10Re	$T_1=1200^\circ\text{C}$ for 1 h, $T_2=1100^\circ\text{C}$ for 20 h	98.5	0.33	305	0.35
	1500°C for 2 h	97.3	2.2	253	0.44
BT	$T_1=1250^\circ\text{C}$ for 1min, $T_2=1050^\circ\text{C}$ for 5 h	97.8	0.18	514	0.36
	1210°C for 2 h	98.0	0.19	459	0.47
BT-BZNT	$T_1=1190^\circ\text{C}$ for 1 min, $T_2=1040^\circ\text{C}$ for 3 h	/	0.52	535	0.48
	1150°C for 3 h	/	0.66	401	0.60